Draft version January 28, 2014
Preprint typeset using LaTeX style emulateapj v. 5/2/11

arXiv:1401.6855v1 [astro-ph.SR] 27 Jan 2014

THE DARKEST SHADOWS: DEEP MID-INFRARED EXTINCTION MAPPING OF A MASSIVE PROTOCLUSTER

Michael J. Butler
Institute of Theoretical Physics, University of Zürich, CH-8057 Zürich, Switzerland

Jonathan C. Tan
Depts. of Astronomy & Physics, University of Florida, Gainesville, FL 32611, USA

Jouni Kainulainen
Max-Planck-Institute for Astronomy, Königstuhl 17, 69117, Heidelberg, Germany
Draft version January 28, 2014

ABSTRACT

We use deep 8μm Spitzer-IRAC imaging of a massive Infrared Dark Cloud (IRDC) G028.37+00.07 to construct a Mid-Infrared (MIR) extinction map that probes mass surface densities up to $\Sigma \sim 1\,\mathrm{g\,cm^{-2}}$ ($A_V \sim 200$ mag), amongst the highest values yet probed by extinction mapping. Merging with a NIR extinction map of the region, creates a high dynamic range map that reveals structures down to $A_V \sim 1$ mag. We utilize the map to: (1) Measure a cloud mass $\sim 7 \times 10^4\,M_\odot$ within a radius of ~ 8 pc. ^{13}CO kinematics indicate that the cloud is gravitationally bound. It thus has the potential to form one of the most massive young star clusters known in the Galaxy. (2) Characterize the structures of 16 massive cores within the IRDC, finding they can be fit by singular polytropic spheres with $\rho \propto r^{-k_\rho}$ and $k_\rho = 1.3 \pm 0.3$. They have $\overline{\Sigma} \simeq 0.1 - 0.4\,\mathrm{g\,cm^{-2}}$ — relatively low values that, along with their measured cold temperatures, suggest magnetic fields, rather than accretion-powered radiative heating, are important for controlling fragmentation of these cores. (3) Determine the Σ (equivalently column density or A_V) probability distribution function (PDF) for a region that is near complete for $A_V > 3$ mag. The PDF is well fit by a single log-normal with mean $\overline{A}_V \simeq 9$ mag, high compared to other known clouds. It does not exhibit a separate high-end power law tail, which has been claimed to indicate the importance of self-gravity. However, we suggest that the PDF does result from a self-similar, self-gravitating hierarchy of structure being present over a wide range of scales in the cloud.
Subject headings: ISM: clouds — dust, extinction — stars: formation

1. INTRODUCTION

Most stars, especially massive ones, form in clusters from dense clumps of gas inside giant molecular clouds (e.g., McKee & Ostriker 2007). Turbulence and magnetic fields are thought to help regulate star formation activity, but both their absolute and relative importance are uncertain. These can affect the overall timescale of star cluster formation, be it dynamically fast (Elmegreen 2007) or slow (Tan et al. 2006), the fragmentation of the gas into self-gravitating cores (Padoan & Nordlund 2002; Vázquez-Semadeni et al. 2005; Kunz & Mouschovias 2009), and thus the mechanism by which massive stars are born, i.e., via competitive clump-fed accretion (Bonnell et al. 2001; Wang et al. 2010) or via core accretion (McKee & Tan 2003), and the stellar initial mass function established.

Progress requires improved observational constraints on the properties of dense gas clumps that are on the verge of massive star and star cluster formation, such as the cold, high column density clouds that reveal themselves as IRDCs, silhouetted against the MIR emission from the Galactic diffuse interstellar medium (e.g., Carey et al. 1998; Rathborne et al. 2006; Butler & Tan 2009). IRDCs suffer from CO freeze out onto dust grains (e.g., Hernandez et al. 2011) and thus have typically been studied via their mm to far-IR (FIR) dust continuum emission (e.g., Rathborne et al. 2006; Peretto et al. 2010). This method has the disadvantage of requiring knowledge of both the emissivity and temperature of dust in the cloud. Single dish observations are needed to recover the total flux, but these have relatively poor angular resolution (e.g. $11''$ FWHM angular resolution for the 1.2 mm observations of Rathborne et al. (2006) with the IRAM 30 m telescope; $\sim 22''$ for the 250μm observations of Peretto et al. (2010) with *Herschel*-SPIRE). Interferometric observations are possible at submm and longer wavelengths, but on their own provide poor constraints on dust temperature.

Extinction mapping is a temperature-independent method to probe cloud structure. However, using background stars in the NIR, clouds are typically only probed up to $A_V \simeq 25$ mag[1] (Kainulainen et al. 2011), while IRDCs can have column densities $\sim 10\times$ larger. Furthermore, the location of IRDCs at $\gtrsim$ kpc distances in the crowded Galactic plane, with NIR sources at a range of distances, necessitates statistical methods that limit the effective angular resolution of

[1] We interchange between Σ, N_H and A_V via $A_V/(1\,\mathrm{mag}) \equiv N_\mathrm{H}/(1.9 \times 10^{21}\,\mathrm{cm^{-2}}) \equiv \Sigma/(4.45 \times 10^{-3}\,\mathrm{g\,cm^{-2}})$ (see Kainulainen & Tan 2013).

the maps to $\sim 30''$.

Thus, MIR extinction (MIREX) mapping has proven more effective at probing IRDCs, e.g. with $2''$ angular resolution achieved with *Spitzer*-IRAC GLIMPSE (Churchwell et al. 2009) 8 μm images (e.g., Butler & Tan 2009). Using the foreground estimation method of Butler & Tan (2012), the maximum Σ that can be probed depends on the noise level of the images: a 1 σ level of 0.6 MJy/sr for GLIMPSE images leads to a maximum, "saturation", mass surface density of $\Sigma_{\rm sat} \sim 0.3 - 0.5$ g cm^{-2} for typical inner Galaxy IRDCs. Since it compares specific intensities towards the IRDC with those of its surroundings, MIREX mapping has difficulties at lower Σ values, where it tends to underestimate true extinctions by $A_V \sim 5 - 10$ mag. This deficiency can be fixed by combining MIR and NIR-derived maps (Kainulainen & Tan 2013).

Here we present an 8 μm extinction map of IRDC G028.37+00.07, hereafter IRDC C (Butler & Tan 2009), with kinematic distance of 5.0 kpc (Simon et al. 2006) made using longer-exposure archival *Spitzer*-IRAC data, probing to $\Sigma_{\rm sat} \simeq 1$ g cm^{-2}. Combining with a NIR extinction map, reveals a very high dynamic range of mass surface densities.

2. METHODS

Butler & Tan (2012) MIREX mapping requires knowing the intensity of radiation just behind the cloud, $I_{\nu,0}$, (estimated by interpolation of surrounding observed intensities) and just in front, $I_{\nu,1}$. Then for negligible emission in the cloud and a 1D geometry, $I_{\nu,1} = e^{-\tau_\nu} I_{\nu,0}$, where optical depth $\tau_\nu = \kappa_\nu \Sigma$, where κ_ν is total opacity at frequency ν per unit total mass. However, foreground emission from the diffuse ISM emission causes us to observe $I_{\nu,1,{\rm obs}} = I_{\nu,{\rm fore}} + I_{\nu,1} = I_{\nu,{\rm fore}} + e^{-\tau_\nu} I_{\nu,0}$ towards the IRDC and $I_{\nu,0,{\rm obs}} = I_{\nu,{\rm fore}} + I_{\nu,0}$ towards the surroundings used to estimate $I_{\nu,0}$.

Following Butler & Tan (2012), we estimate $I_{\nu,{\rm fore}}$ by searching for saturation in independent cores, occurring when Σ is large enough to block essentially all background emission. Butler & Tan (2012) used *Spitzer* GLIMPSE data with 2.4s exposures. We now use archival data of IRDC C (PI G. Fazio; Project ID DARKCLOUDS/219; AOR key 6050304), with 10.4 s exposure per pointing. After starting with PostBCD data (pipeline version S18.18.0), the final combined image consists of 12 mosaiced $5.2' \times 5.2'$ pointings, resulting in ~ 20 regions that have different total exposures, 1σ noise and instrumental background levels (Figure 1a). For each region with area $\gtrsim$500 pixels, we search for saturation by: (1) Find $I_{\nu,1,{\rm obs}}({\rm min})$, the minimum value of $I_{\nu,1,{\rm obs}}$. (2) Find all pixels with $I_{\nu,1,{\rm obs}}({\rm min}) < I_{\nu,1,{\rm obs}} < I_{\nu,1,{\rm obs}}({\rm min}) + 2\sigma$. If these are spatially independent (i.e., extended over $\geq 4''$, cf. $8''$ of Butler & Tan (2012)), then the region is defined to exhibit "local saturation" and all pixels in this intensity range are labeled "saturated". Steps 1 and 2 are repeated for each region. (3) Evaluate the mean value of $I_{\nu,1,{\rm obs}}$ of saturated pixels in all regions, $I_{\nu,1,{\rm obs}}({\rm sat})$ (in practice only 2 regions exhibit saturation, see §3.2). Apply an offset to each saturated region equal to the difference between $I_{\nu,1,{\rm obs}}({\rm sat})$ and its local value. We expect these offsets result from varying instrumental background noise. We then subtract a local 2σ intensity from the foreground to each region, which ensures every pixel has a finite estimate of Σ. The average estimate of $I_{\nu,{\rm fore}}$ is $\simeq 31.2$ MJy/sr ($\simeq 0.6$ MJy/sr greater than the Butler & Tan (2012) value). Lack of areal coverage of the archival data means we must use the background model derived from GLIMPSE (Butler & Tan 2012). This was scaled to match intensities of the archival data by comparing median intensities in several small patches free of stellar or extended emission sources, which were used to derive a single mean offset factor.

Longer integration times (everywhere $\geq$ 10.4 s; all identified core/clumps [§3.2] have $\geq$ 20.8 s, up to maximum of 52 s; compared to 2.4 s for GLIMPSE), cause the 1σ noise level to fall from ~ 0.6 MJy/sr (Reach et al. 2006) to $0.29, 0.20, 0.14$MJy/sr for the $10.4, 20.8, 41.6$s exposure regions, respectively. While the absolute value of this noise level is somewhat uncertain, the relative values should be better determined. By subtracting a 2σ noise level, our method sets the minimum value of $I_{\nu,1} \simeq 1 - 2\sigma$, leading to a limit at which our Σ measurements begin to be underestimated by saturation effects, $\Sigma_{\rm sat} = \tau_{\nu,{\rm sat}}/\kappa_\nu = \ln(I_{\nu,0}/I_{\nu,1})/\kappa_\nu$, of $0.625, 0.675, 0.722$ g cm^{-2} respectively, assuming $I_{\nu,1} = 2\sigma$ and a value of $I_{\nu,0} = I_{\nu,0,{\rm obs}} - I_{\nu,{\rm fore}} = (94.3 - 31.2 = 63.1)$ MJy/sr, the mean intensity of our scaled background model with foreground subtracted. This represents an increase of up to $\sim$40% in dynamic range compared to the Butler & Tan (2012) map, which had $\Sigma_{\rm sat} \simeq 0.5$ g cm^{-2}. A true Σ value that is equal to $\Sigma_{\rm sat}$ is underestimated by about 7% (cf. 17% for Butler & Tan 2012). Thus the new map not only probes to higher Σ, but does so with greater accuracy. Note, values of $\Sigma > \Sigma_{\rm sat}$ are present in the map, up to ~ 0.85 g cm^{-2}.

The above equation for $\Sigma_{\rm sat}$ is also useful for seeing the effect of errors in estimating the background specific intensity, $I_{\nu,0}$. This is expected to show fluctuations about the median interpolated level: Butler & Tan (2009) find the HWHM of the distribution of background intensities around IRDC C to be a factor of 1.2. This introduces an error of $\Delta\Sigma = (\ln 1.2)/\kappa_\nu \rightarrow 0.024$ g cm^{-2}, which is only a $\sim 3-4$% error for $\Sigma \simeq \Sigma_{\rm sat}$, growing to 20% in the optically thin limit.

In several locations, Σ "holes" are seen, where Σ is significantly lower than the surrounding pixels. This could be caused by the presence of a real MIR-bright point source or by an instrumental artifact, such as a bad pixel. To identify the latter, we use the original GLIMPSE 8μm image as a reference. If there is no source in the GLIMPSE image, then the hole in the new image is corrected by replacing the bad pixel with the mean of the nearest unaffected pixels. This typically occurs far from any of the centers of our core sample (§3.2), with the exception of C1, which had a hole directly adjacent to core center.

Finally, we follow Kainulainen & Tan (2013) to merge the MIREX map with a NIR extinction map of the region, derived using the method of Kainulainen et al. (2011) and data from the *UKIRT/Galactic Plane Survey* (Lawrence et al. 2007). The technique estimates NIR extinction towards background stars by comparing their NIR colors to those of stars in a nearby reference field. The zero-point calibration uncertainty is estimated to be $A_V \sim 1$ mag. To combine the

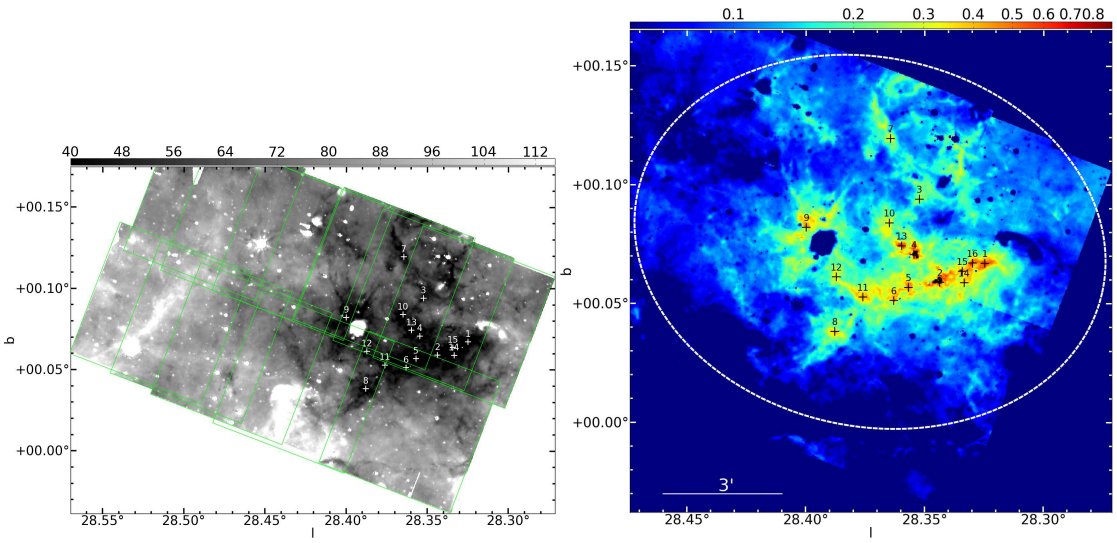

FIG. 1.— *(a) Left*: 8μm image of IRDC G028.37+00.07 (Cloud C) with intensity scale in MJy/sr. Dotted squares show the 12 *Spitzer* IRAC pointings, each with 10.4 s exposure, used to construct the mosaiced image. *(b) Right*: Merged NIR+MIR Σ map (units of g cm^{-2}). The IRDC-defining ellipse from Simon et al. (2006) is shown. Core/clump centers (§3.2) are labeled with crosses. Saturated pixels are marked with white squares.

NIR and MIR extinction maps, a relative dust opacity-law of $\tau_{8\mu\mathrm{m}} = 0.29\tau_K$ is adopted (Kainulainen & Tan 2013). The net effect of the combination is a zero point shift of the MIREX map by $A_V \sim 5-10$ mag, which varies at the resolution of the NIR map of 30″. In regions where $A_V \gtrsim 15$ mag, the NIR map is not accurate so we interpolate its value from surrounding regions. The final combined map is shown in Figure 1b.

3. RESULTS

3.1. *Overall Cloud Mass and Dynamics*

Inside the IRDC elliptical boundary of Simon et al. (2006) (effective radius of $R_{\rm eff} = 7.7$ pc, $e = 0.632$) the mean mass surface density is $\overline{\Sigma} = 0.0926\,\mathrm{g\,cm^{-2}}$ (ignoring regions affected by MIR-bright sources). We assume a 30% uncertainty due to the opacity per unit mass, which includes dust opacity and dust-to-gas mass ratio uncertainties (Butler & Tan 2012). This result is 28% higher than the value of $\overline{\Sigma} = 0.0721\,\mathrm{g\,cm^{-2}}$ from (Kainulainen & Tan 2013), which we attribute to the new map's ability to probe to higher values of Σ.

Given $\overline{\Sigma}$ and the kinematic distance of 5.0 kpc, for which we assume 20% uncertainty, the total IRDC mass inside the ellipse is $M = 6.83\times10^4\,M_\odot$, with 50% overall uncertainty. This compares with our previous estimate of $5.32\times10^4\,M_\odot$ (Kainulainen & Tan 2013). This shows that IRDC C is one of the more massive molecular clumps in the Galaxy. Its mass is comparable to the 1.1 mm Bolocam Galactic Plane Survey (BGPS) clumps of Ginsburg et al. (2012) and the $1.3\times10^5\,M_\odot$, 2.8 pc-radius Galactic center clump (the "Brick") of Longmore et al. (2012). Note that these masses are based on dust continuum emission and thus suffer from additional uncertainties due to dust temperature estimates. With this caveat in mind, these massive mm clumps appear to be a factor of about 10 denser than IRDC C, which, inside $R_{\rm eff}$, we estimate to be $n_{\rm H} \simeq 1120\,\mathrm{cm^{-3}}$ (but with the caveat of assuming spherical geometry), corresponding to a free-fall time of $t_{\rm ff} = [3\pi/(32G\rho)]^{1/2} = 1.30\times10^6$ yr. Apart from the Brick, the mm clumps are typically already undergoing active star formation. Some stars have started to form in IRDC C (e.g. the MIR-bright sources; see also Zhang et al. 2009), but overall the star formation activity appears to be relatively low, and so this cloud should represent an earlier stage of massive star cluster formation.

From ^{13}CO(1−0) Galactic Ring Survey data (Jackson et al. 2006), the IRDC's 1D velocity dispersion, σ, (integrating over the Simon et al. (2006) ellipse) is $3.41-3.75\,\mathrm{km\,s^{-1}}$ (depending on method of gaussian fitting or total integration, Kainulainen & Tan 2013). If the cloud is virialized, then σ should be $4.2\mathrm{km\,s^{-1}}$ (ignoring surface pressure and magnetic field terms and evaluated for a spherical cloud with internal power law density profile of $\rho \propto r^{-k_{\rho,\rm cl}}$ with $k_{\rho,\rm cl} = 1$; Bertoldi & McKee 1992). Support by large scale magnetic fields would reduce the virial equilibrium velocity dispersion, although such support is unlikely to be dominant given an expected field strength of 12 μG implied by the cloud's mean density (Crutcher et al. 2010). Thus, overall the cloud appears close to virial equilibrium (or perhaps sub-virial), implying it is gravitationally bound and that self-gravity is important over the largest size scales defining the cloud.

3.2. *Internal Structure of Cores and Clumps*

The properties of 9 dense core/clumps (C1-C9) within the IRDC were studied by Butler & Tan (2012). We now expand the sample, to obtain a more complete census of the massive starless or early-stage core/clumps in the cloud, identifing 7 new core/clumps (C10-C16): these are the 7 highest Σ local maxima external to C1-C9. They are also required to be free of 8 μm sources. Zoomed-in views of the cores are presented in Figure 2.

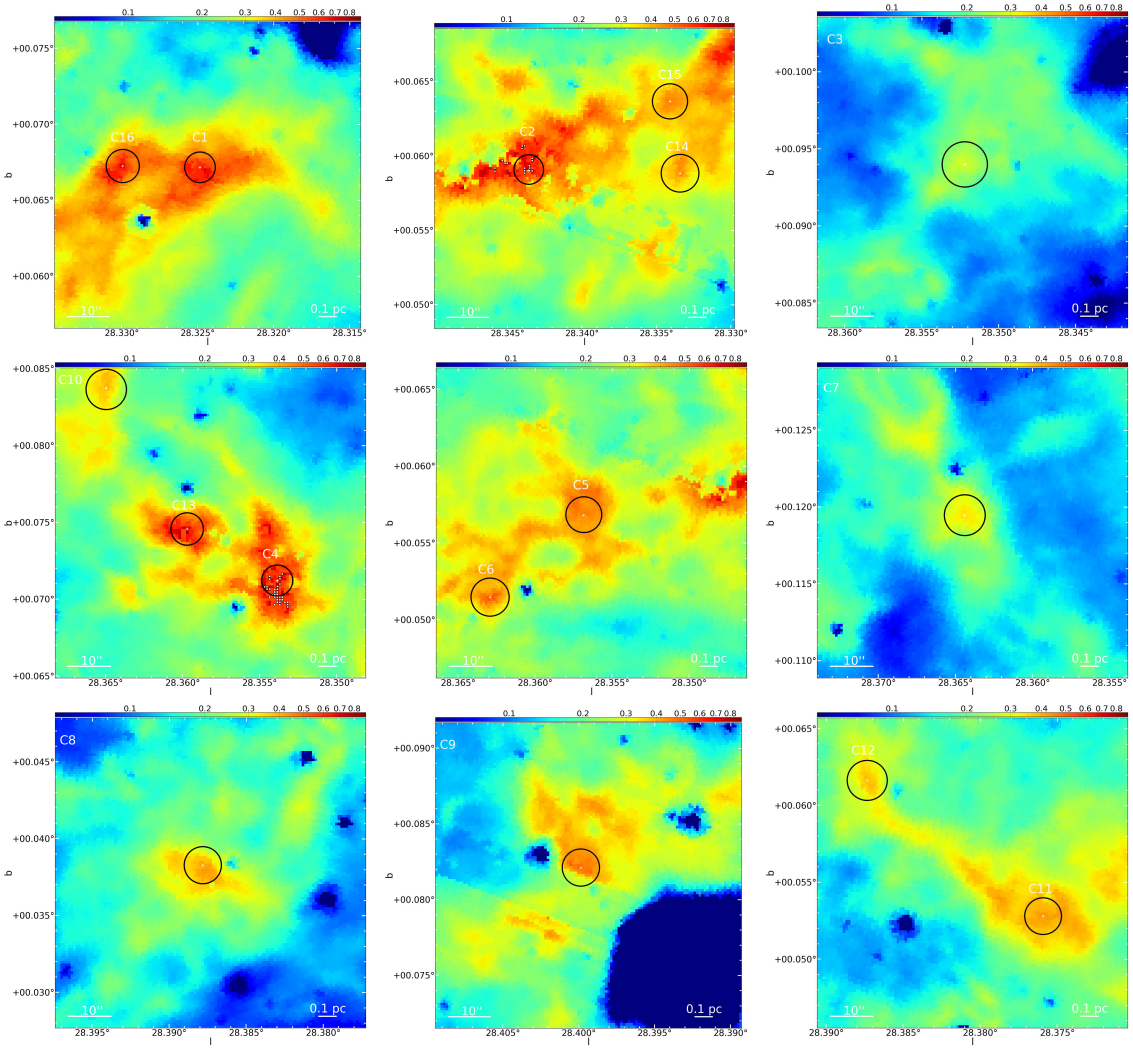

FIG. 2.— Zoom images of 9 regions from Fig. 1b, illustrating 16 identified core/clumps. *Top row, left to right:* (a) C1, C16; (b) C2, C14, C15; (c) C3. *Middle row, left to right:* (d) C4, C10, C13; (e) C5, C6; (f) C7. *Bottom row, left to right:* (g) C8; (h) C9; C11, C12. For each core/clump, the black circle shows the region enclosing 60 $M_\odot$. White squares mark saturated pixels, present in C2 and C4 (see text).

Only C2 and C4 exhibit saturation as defined in §2. Following Butler & Tan (2012), we use the unsaturated portions of the Σ profiles to derive the power law volume density structure of the core/clumps, $\rho_{\rm cl}(r) = \rho_{\rm s,cl}(r/R_{\rm cl})^{-k_{\rho,{\rm cl}}}$, where $\rho_{\rm s,cl} = \mu_{\rm H} n_{\rm H,s,cl}$ (with $\mu_{\rm H} = 2.34\times10^{-24}$ g) is the density at the surface of the core/clump, $R_{\rm cl}$. We hereafter refer to these objects as "clumps". We also consider background-subtracted Σ profiles, where a uniform average background is evaluated from the annulus from $R_{\rm cl}$ to $2R_{\rm cl}$, and describe these objects as "cores".

We first consider the properties of the core/clumps at a scale that encloses $M_{\rm cl} = 60\,M_\odot$, which is approximately the mass scale needed to form a massive (O) star (McKee & Tan 2003). We find the mean/median/dispersion of the $k_{\rho,{\rm cl}}$ values are 0.826/0.775/0.262. Equivalently, for the envelope-subtracted cores we find $k_{\rho,c}$ mean/median/dispersion values of 1.33/1.39/0.299. These are similar to the Butler & Tan (2012) results. The mean core mass is $M_c = 14.9\,M_\odot$, so the method of envelope subtraction typically removes about 3/4 of the total mass that is projected along the line of sight. Envelope subtraction depends on the assumed 3D geometry of the core and its surrounding clump and so is quite uncertain. Astrochemical tracers of starless cores, such as N_2D^+, are thus useful for helping to locate these objects more precisely (Tan et al. 2013).

The mean/median/dispersion values for Σ of the 60 $M_\odot$ clumps are 0.446/0.424/0.109 g cm^{-2} and for the cores are 0.118/0.107/0.0938 g cm^{-2}. If core properties are better estimated after envelope subtraction, then their Σ's are relatively small, e.g. compared to fiducial values of the turbulent core model of massive star formation (McKee & Tan 2003) with $\Sigma \sim 1$ g cm^{-2} or the hypothesized minimum Σ threshold for massive star formation of 1 g cm^{-2} due to accretion powered heating suppression of fragmentation Krumholz & McKee (2008). Even if the maximum values, i.e. with no envelope subtraction, are assigned to the cores, then these are still somewhat smaller than 1 g cm^{-2}. Note, that these 16 cores are amongst the highest Σ peaks in the extinction map. Note also, that at least some (e.g., C1) and probably most of the cores are very cold ($\sim 10-15$ K) (Wang et al. 2008; Tan et al. 2013), so radiative heating is

TABLE 1
Structural Properties of Core/Clumps[a]

Name	l (°)	b (°)	$R_{\rm cl}=R_c$ (pc)	$\bar{\Sigma}_{\rm cl}$ (g cm^{-2})	$\bar{\Sigma}_c$ (g cm^{-2})	$k_{\rho,{\rm cl}}$	$k_{\rho,c}$	$n_{\rm H,s,cl}$ (10^5cm^{-3})	$n_{\rm H,s,c}$ (10^5cm^{-3})	$M_{\rm cl}$ ($M_\odot$)	$M_{\rm c}$[b] ($M_\odot$)
C1	28.32450	0.06655	0.0806	0.613	0.141	1.06	1.53	5.84	0.951	60.0	13.7
			0.0581	0.637	0.151	1.06	1.58	5.38	1.27	32.4	7.70
C2	28.34383	0.06017	0.0793	0.633	0.254	1.18	1.86	6.18	2.13	60.0	24.1
			0.0872	0.630	0.246	1.14	1.50	3.75	1.46	72.2	28.2
C3	28.35217	0.09450	0.120	0.276	0.0200	0.775	1.18	1.51	0.0822	60.0	4.36
			0.0581	0.287	0.0257	0.740	1.36	2.80	0.251	14.6	1.31
C4	28.35417	0.07067	0.0806	0.614	0.335	1.36	1.95	6.04	2.67	60.0	32.7
			0.101	0.607	0.274	1.36	1.82	2.43	1.10	94.6	42.8
C5	28.35617	0.05650	0.0942	0.449	0.0575	0.538	0.979	3.73	0.371	60.0	7.67
			0.0872	0.453	0.0670	0.5200	0.600	4.31	0.637	51.8	7.70
C6	28.36267	0.05150	0.100	0.392	0.179	0.777	1.42	3.28	1.28	60.0	27.4
			0.843	0.315	0.0951	0.800	1.14	0.240	0.0725	3370	1020
C7	28.36433	0.11950	0.108	0.338	0.0494	0.759	1.08	2.26	0.247	60.0	8.75
			0.0581	0.356	0.0558	0.680	1.14	3.94	0.616	18.1	2.84
C8	28.38783	0.03817	0.0979	0.415	0.226	1.10	1.57	2.87	1.21	60.0	32.6
			0.218	0.368	0.143	1.02	1.70	0.759	0.296	263	103
C9	28.39950	0.08217	0.0997	0.401	0.0496	0.707	1.14	3.64	0.331	60.0	7.43
			0.0872	0.405	0.0553	0.740	1.14	2.98	0.408	46.3	6.34
C10	28.36486	0.08397	0.107	0.346	0.0456	0.737	1.23	2.66	0.235	60.0	7.90
			0.0872	0.351	0.0508	0.480	1.12	2.61	0.378	40.2	5.82
C11	28.37600	0.05279	0.0968	0.424	0.107	0.563	0.920	3.47	0.729	60.0	15.1
			0.130	0.421	0.100	0.520	0.980	2.24	0.536	108.	25.9
C12	28.38717	0.06128	0.106	0.352	0.0450	0.900	1.42	2.62	0.279	60.0	7.66
			0.0581	0.370	0.0564	0.860	1.64	2.99	0.455	18.8	2.87
C13	28.33317	0.05900	0.0846	0.557	0.180	1.04	1.47	5.2	1.40	60.0	19.4
			0.0872	0.555	0.198	1.00	1.56	3.17	1.13	63.6	22.7
C14	28.33401	0.06383	0.103	0.374	0.0408	0.383	1.07	2.87	0.261	60.0	6.54
			0.130	0.372	0.0445	0.360	0.720	2.24	0.268	95.9	11.4
C15	28.33418	0.06366	0.0956	0.435	0.136	0.621	1.39	3.60	0.938	60.0	18.7
			0.290	0.409	0.0994	0.160	1.00	0.974	0.236	521	126
C16	28.32985	0.06717	0.0878	0.516	0.0350	0.710	1.09	4.65	0.263	60.0	4.07
			0.0581	0.521	0.0344	0.620	1.10	5.88	0.389	26.5	1.75
Mean			0.0963	0.446	0.118	0.826	1.33	3.78	0.836	60.0	14.9
			0.152	0.441	0.106	0.754	1.26	2.92	0.594	302	88.5
Median			0.0979	0.424	0.107	0.775	1.39	3.60	0.729	60.0	13.7
			0.0872	0.409	0.0951	0.740	1.14	2.98	0.455	63.6	11.4
Dispersion			0.0115	0.109	0.0938	0.262	0.299	1.41	0.750	0.00	9.84
			0.195	0.114	0.0763	0.313	0.353	1.54	0.417	828	251

[a] First line for each source shows results at the scale where the total projected enclosed mass is $M_{\rm cl}=60\,M_\odot$; second line shows results at the "best-fit" scale, minimizing the reduced χ^2 of the projected power law density fit to the $\Sigma(r)$ profile.
[b] Based on fitted power law density profile, which compensates for mass missed in saturated core centers, i.e. relevant for C2 and C4, typically $\lesssim 10\%$ of total.

not currently suppressing their fragmentation. Magnetic suppression of fragmentation of these core/clumps, requiring $\sim 0.1-1$ mG fields, remains a possibility (Butler & Tan 2012; Tan et al. 2013).

The structural properties of the core/clumps at the $M_{\rm cl}=60\,M_\odot$ scale are summarized in Table 1. Also shown here are the results of a more general fitting of power-law density profiles where the outer radius is varied and the reduced χ^2 of the fit minimized (Butler & Tan 2012). Sometimes the best-fit model is quite close the $M_{\rm cl}=60\,M_\odot$ model, but in other cases it can shrink somewhat or grow up to $\sim 10^3\,M_\odot$. The roughly similar structural properties over a range of length and mass scales may indicate that there is a self-similar hierarchy of structure present in the IRDC. At the same time we caution that the "best-fit" model is often not that much better than models fit to other scales. Nonspherical geometries can also be important, which can limit the applicability of these simple spherical models.

3.3. *The Mass Surface Density Probability Distribution Function*

The Σ (or A_V or $N_{\rm H}$) PDF, either area ($p_A(\Sigma)$) or mass-weighted ($p_M(\Sigma)$), entrains information about cloud self-gravity, turbulence, shocks and magnetic field support. Our temperature-independent high-dynamic range extinction map can yield the best constraints on the Σ PDF. However, the relatively limited areal coverage of the archival *Spitzer* data require us to utilize the GLIMPSE-based maps of Kainulainen & Tan (2013) (offset-corrected to smoothly join the new map) to extend the region to completely cover a $20'\times19'$rectangular area that encloses an $A_V=3$mag contour (cf. the $15'\times15'$ area enclosing the $A_V=7$ mag contour of Kainulainen & Tan 2013).

The area and mass-weighted Σ PDFs are shown in Fig. 3. The new PDF extends to both lower and higher values of Σ compared to that derived by Kainulainen & Tan (2013). We fit a log-normal function to $p_A(\ln\Sigma)$, and then use this to derive $\overline{\ln\Sigma}$ (over the considered range of Σ), which then defines the mean $\overline{\Sigma}_{\rm PDF}\equiv e^{\overline{\ln\Sigma}+\sigma^2_{\ln\Sigma}/2}$, where $\sigma_{\ln\Sigma}$ is the standard deviation of $\ln\Sigma$ (note typo in eq. 26 of Kainulainen & Tan 2013), used to define the mean-normalized

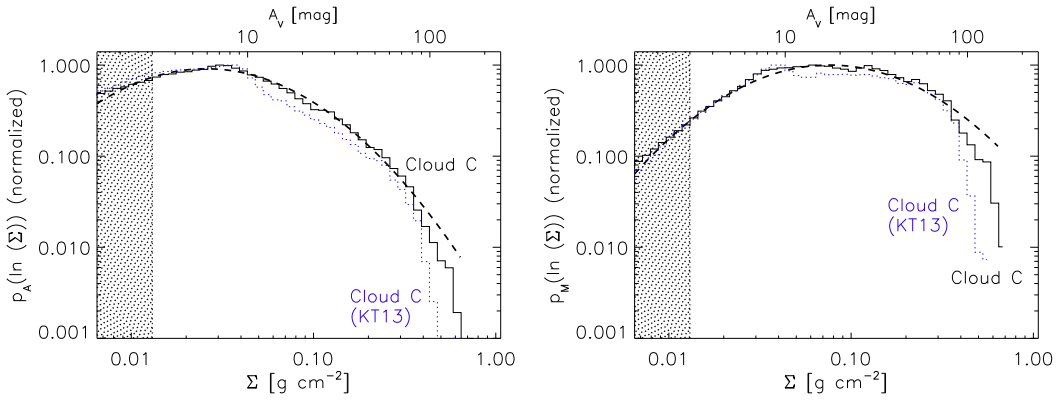

FIG. 3.— *(a) Left:* Area-weighted probability distribution function of Σ for IRDC G028.37+00.07 (Cloud C) (black histogram) and best-fit log-normal (dashed line) covering a contiguous region completely enclosing an $A_V > 3$ mag contour — above this level, shown by the shaded/nonshaded boundary, the PDF is complete, modulo saturation effects for $A_V \gtrsim 200$ mag. We also show the Kainulainen & Tan (2013)-derived PDF (purple histogram), based on a shallower, smaller dynamic range extinction map. *(b) Right:* Mass-weighted PDFs, with same notation as (a).

mass surface density, $\Sigma' \equiv \Sigma/\overline{\Sigma}_{\rm PDF}$. For this distribution, we find the best-fit log-normal

$$p_A(\ln\Sigma') = \frac{1}{(2\pi)^{1/2}\sigma_{\ln\Sigma'}}\exp\left[-\frac{(\ln\Sigma' - \overline{\ln\Sigma})^2}{2\sigma^2_{\ln\Sigma'}}\right], \quad (1)$$

where $\sigma_{\ln\Sigma'}$ is the standard deviation of $\ln\Sigma'$. We find $\overline{\Sigma}_{\rm PDF} = 0.039\,{\rm g\,cm^{-2}}$ (i.e. $\overline{A}_{V,\rm PDF} = 9.0$ mag) and $\sigma_{\ln\Sigma'} = 1.4$, compared with 8.3 mag and 1.7 found by Kainulainen & Tan (2013), respectively. Note, Kainulainen & Tan (2013) only fit to $A_V > 7$ mag, insufficient to determine the PDF peak so the parameters of their log-normal fit are less accurate.

The derived PDF is well fit by a single log-normal. Deviation at high $\Sigma \gtrsim 0.5\,{\rm g\,cm^{-2}}$ may be due to saturation (§2) or absence of MIR-bright high Σ regions. The value of $\overline{A}_{V,\rm PDF}$ is much higher than in nearby star-forming clouds ($\overline{A}_{V,\rm PDF} \simeq 0.6 - 3.0$ mag) (Kainulainen et al. 2009). G028.37+00.07 also has a higher dense gas fraction than other studied IRDCs (e.g., Kainulainen & Tan 2013). The PDF shows no indication of a high-end power law tail (indeed there is no room for such a tail if the PDF peak is dominated by the log-normal), observed in some clouds (e.g., Kainulainen et al. 2011) and modeled as being due to a separate self-gravitating component (e.g., Kritsuk et al. 2011) (however, see Kainulainen et al. 2011b). Since the observed line-widths (§3.1) indicate the overall cloud is self-gravitating, this may imply that a self-similar, self-gravitating hierarchy of structure is present over the complete range of spatial scales in the cloud probed by our extinction map and that such a hierarchy produces a log-normal-like Σ PDF (see also Goodman et al. 2009). This needs to be explored in global (non-periodic box) simulations of magnetized, self-gravitating molecular clouds.

We thank the referee for helpful comments. We acknowledge NASA grant ADAP10-0110 (JCT) and Deutsche Forschungsgemeinschaft program 1573 (JK).

REFERENCES

Bonnell, I.A., Clarke, C.J., Bate, M.R. et al. 2001, MNRAS,324,573
Bertoldi, F. & McKee, C.F. 1992, ApJ,395,140
Butler M.J., & Tan J.C. 2009, ApJ,696,484
Butler M.J., & Tan J.C. 2012, ApJ,754,5
Carey, S.J., Clark, F.O., Egan, M.P. et al. 1998, ApJ,508,2
Crutcher, R.M., Wandelt, B., Heiles, C. et al. 2010, ApJ,725,466
Churchwell, E., Babler B., Meade, M. et al. 2009, PASP,121,213
Elmegreen, B.G. 2007, ApJ,663,743
Ginsburg, A., Bressert, E., Bally, J. et al. 2012, ApJ,758,L29
Goodman, A.A., Rosolowsky, E.W., Borkin, M.A. et al. (2009), Nature,457,63
Hernandez, A.K., Tan, J.C., Caselli, P. et al. 2011, ApJ,738,11
Jackson, J.M., Rathborne, J.M., Shah, R.Y., et al. 2006, ApJS,163,145
Kainulainen, J., Alves, J., Beuther, H., et al. 2011a, A&A,536,A48
Kainulainen, J., Beuther, H., Banerjee, R. et al. 2011b, A&A,530,A64
Kainulainen, J., Beuther, H., Henning, T., & Plume, R. 2009, A&A,508,L35
Kainulainen, J., & Tan, J.C. 2013, A&A,549,A53
Kritsuk, A.G., Norman, M.L. & Wagner, R. 2011, ApJ,727,L20
Krumholz, M.R. & McKee, C.F. 2008, Nature,451,1082
Kunz, M.W., & Mouschovias, T. Ch. 2009, MNRAS,399,L94
Lawrence, A., Warren, S.J., Almaini, O., et al. 2007, MNRAS,379,1599
Longmore, S.N., Rathborne, J., Bastian, N. et al. 2012, ApJ,746,117
McKee, C.F., & Ostriker, E.C. 2007, ARA&A,45,565
McKee, C.F., & Tan, J.C. 2003, ApJ,585,850
Padoan, P., & Nordlund, A. 2002, ApJ,576,870
Peretto N., Fuller G.A., Plume R. et al. 2010, A&A,518,L98
Rathborne, J.M., Jackson, J.M., & Simon, R. 2006, ApJ,641,389
Reach, W.T., Rho, J., Tappe, A., et al. 2006, AJ,131,1479
Simon, R., Rathborne, J.M., Shah, R.Y. et al. 2006, ApJ,653,1325
Tan, J.C., Krumholz, M.R., & McKee, C.F. 2006, ApJ,641,L121
Tan J.C., Kong S., Butler M.J. et al. 2013, ApJ,779,96
Vázquez-Semadeni, E., Kim, J., & Ballesteros-Paredes, J. 2005, ApJ,630,L49
Wang, Y., Zhang, Q., Pillai, T. et al. 2008, ApJ,672,L33
Wang, P., Li, Z-Y., Abel, T. et al. 2010, ApJ,709,27
Zhang Q., Wang Y., Pillai T. et al. 2009, ApJ,696,268